Size-dependent scaling of capillary invasion including buoyancy and pore size distribution effects

Lee M. Hirsch and Arthur H. Thompson

Exxon Production Research Company, P.O. Box 2189, Houston, Texas 77252-2189

The effect of sample size on fluid saturation during capillary invasion is determined by modeling the invasion process on three-dimensional cubic networks consisting of pore throats with radii randomly selected from various pore size distributions. Without buoyancy, the threshold saturation of the nonwetting fluid when it completes a connected path across a sample decreases with the square root of sample size for all the pore size distributions studied. Experiments on Berea sandstone samples ranging from 0.3 to 30 cm in size confirm the $1/\sqrt{L}$ scaling relation. The $1/\sqrt{L}$ scaling is the prediction of percolation theory without buoyancy. Large-aspect-ratio [(height):(diameter)] samples have greater threshold nonwetting phase saturations than low-aspect-ratio samples. Relative permeability, which is dependent on the largest interconnected pores, also depends on sample size and shape. The pore size distribution affects the pore occupancy when buoyancy is important. To describe this effect we introduce a measure of the skewness of the pore size distribution into the Bond number (the Bond number B is the ratio of buoyancy to capillary pressures). For all the cases examined, a universal scaling law for the threshold saturation has been found based on the ratio of sample size L to Bond number correlation length ξ_B. ξ_B is proportional to $B^{-0.47}$. This scaling relation incorporates the effects of fluid density contrast, pore size distribution, surface tension, and contact angle while retaining the basic Bond number scaling previously predicted for percolation on lattices with uniform (flat) pore size distributions. The height of the critical pore that must be filled to achieve breakthrough of the nonwetting phase is a useful parameter that also scales with L/ξ_B. These finite-size scaling results have important implications for models of oil migration to reservoirs and models of pollutant migration in ground water.

PACS number(s): 47.55.Mh, 47.53.+n, 91.60.−x

I. INTRODUCTION

The flow of immiscible fluids in porous media is central to numerous technologically important processes. In both the formation and production of petroleum reservoirs one fluid is displaced by another in a porous medium, the sedimentary rock. When pollutants migrate in soils a nonaqueous liquid phase displaces ground water. The escape of gas from radioactive waste repositories occurs when gas displaces water from a porous rock. Interest in these and similar problems has led to numerous theoretical and experimental studies of the fundamental processes. In the higher velocity flow regimes macroscopic fluid instabilities such as viscous fingering are seen. When the flow is very slow viscous forces can be neglected and the dynamics are dominated by capillary and buoyancy forces. The slow flow regime is important to the migration of oil to and from a reservoir and to the pollution migration problems. In this study we are interested in the slow flow, capillary pressure dominated regime and in particular the size-dependent scaling of the flow.

The slow displacement of one fluid by another from a porous medium is now recognized to be a special problem in percolation known as invasion percolation [1–3]. In invasion percolation only pores connected to the invading front are filled. Several papers have discussed invasion percolation in porous media in the presence of a buoyancy pressure gradient [4–7]. These papers have concentrated on the case where the capillary pressures are much less than the buoyancy pressures. Under those conditions the light invading fluid rises rapidly upward in a column of "blobs" where each blob has a size characteristic of the percolation coherence length. The fraction of occupied bonds averaged over the height of the column is typically 10–20%. In this paper we consider a problem that is more representative of the physical conditions expected in the slow migration of oil from a source rock to a reservoir, a process known as secondary migration. (Primary migration is the migration of oil or gas out of a source rock, such as a shale, into a carrier rock that might be a sandstone, for example.) Our work is also applicable to the slow migration of other nonaqueous phases into water-saturated porous media.

The problem we model is a porous medium filled with wetting fluid overlying a source of nonwetting fluid. The nonwetting fluid slowly enters the bottom face of the porous medium and at each point in time reaches capillary equilibrium. The pressure in the nonwetting fluid is permitted to rise to whatever value is necessary to overcome capillary pressures. The capillary pressures are assumed to be so large that the buoyancy pressure does not spontaneously cause completion of the first connected path of nonwetting fluid, i.e., the sample is smaller than the percolation coherence length.

The results of our model calculation lead to conclusions about the expected field-scale saturations and flow rates that are in substantial disagreement with the conventional assumptions used in geological basin modeling. In particular, we expect that the threshold satura-

tions for migration of hydrocarbons in the cited applications will be substantially smaller and the flow rates substantially higher than usually assumed.

Network simulations of invasion percolation have been extensively used to represent the slow displacement of a wetting fluid in a porous medium [3,8,9]. At breakthrough, i.e., when the invading fluid spans the network, the invaded fluid structure is a percolation cluster of fractal dimension 2.5 [1,8]. The mass of the percolation cluster thus scales as $L^{2.5}$ while the total volume scales as L^3. Thus the saturation varies with the size dimension as $L^{2.5}/L^3 = L^{-1/2}$. This result suggests that saturation in secondary migration could be very small on the basin scale of hundreds to thousands of meters. Both the scale dependence and the possibility of low saturation at the scale of geological basins contradict the conventional wisdom for secondary migration, which has been that oil saturations must be relatively high, e.g., 10–15%. High saturation estimates are based on capillary invasion experiments at high flow rates in glass bead packs or from capillary breakthrough experiments on small ($\sim$2 cm) cores [10]. The high saturations are often erroneously reinforced by the expected $\sim$15% saturation in ordinary percolation, which does not apply to this invasion situation.

In the Earth, the effect of gravity must also be considered. When a rock that is saturated with high density fluid is injected from below by a low-density nonwetting fluid, the hydrostatic pressure adds to the injection pressure and creates a vertical gradient in the effective injection pressure. The fraction of accessible pores increases with height. Wilkinson [1] showed that the length scale over which percolation fractal behavior is observed decreases with increasing buoyancy. In addition, Wilkinson showed that when invasion of a lattice proceeds by selecting the largest accessible pore at each step, the saturation decreases with buoyancy. Many similar studies have been done [4,5,9], but few have systematically studied the influence of pore size distribution and buoyancy.

We simulate the invasion of nonwetting fluid into rocks of various sizes with three-dimensional cubic lattices. When a connected pathway of nonwetting fluid first forms between the ends of the sample, occupation of the lattice without buoyancy is proportional to $L^{-1/2}$, as predicted for the percolation problem. The size of the critical pore that must be filled for breakthrough to occur is relatively insensitive to sample size. We specifically identify and determine the saturation of the filled "pretender" paths that are not connected to the percolation cluster at breakthrough. Our experimental results for invasion display the $L^{-1/2}$ dependence of saturation over the range of sample sizes from 0.3 to 30 cm. We also present saturation data on a rock with highly anisotropic structure and show that the saturation is consistent with two-dimensional percolation. To describe how pore size distribution affects the influence of buoyancy on saturation, we incorporate a measure of the skewness of a pore size distribution into the Bond number (the ratio of buoyancy to capillary pressures). The new Bond number is related to the correlation length over which the invaded structure is fractal in the manner described using invasion per-

colation theory by Wilkinson [1,2]. For sample sizes of the order of this correlation length, buoyancy effects are shown to be negligible. In both our experiments and simulations, we consider the range of relatively small Bond numbers between 10^{-5} and 0.05. This contrasts with most experimental studies that typically have Bond numbers in the range 0.01–0.8 [6,7]. Small Bond numbers are more characteristic of problems in secondary migration and possibly critical gas saturation. For our conditions we show that buoyancy enhances saturation. The relative height of the critical pore that must be filled for breakthrough also depends on the Bond number. We show that saturation is dependent on the aspect ratio of the sample. Our experimental results suggest that relative permeability at breakthrough depends on sample size and shape.

The simulations show that the buoyancy effects depend on the pore size distribution. Pore size distributions that reflect those expected in rocks are skewed toward small pore sizes. In these distributions the effects of buoyancy are substantially reduced. These results suggest that simulations on uniform (flat) pore size distributions and experiments on bead packs will not accurately model rock behavior.

Our choice of boundary conditions and the use of capillary equilibrium differs from many similar studies [8,9], which attempt to incorporate dynamic effects of invasion into percolation models. The differing methods produce identical invaded structures as the percolation threshold is approached; however, saturations at breakthrough will differ. The choice of appropriate conditions for applications depends on the detailed characteristics of the modeled process. However, our description of the effect of pore size distribution on Bond number, correlation length, and the height of the critical pore that must be filled for breakthrough generally applies.

We do not confine ourselves to the situation of oil invading water-saturated porous media. We consider large and small density contrasts as well as examples of negative buoyancy, i.e., a dense nonwetting fluid entering from the base of the rock. Thus the results are equally applicable to the migration of oil through water such as in secondary migration, the migration of gas through oil such as in the critical gas saturation of importance in reservoir engineering, the migration of gas through water such as in air sparging techniques for remediation of polluted soil [11] or from a radioactive waste repository, and mercury injection experiments. We report experimental results on both oil invasion and mercury injection.

II. DESCRIPTION OF CAPILLARY INVASION SIMULATIONS

We model the capillary invasion of nonwetting fluid into a rock saturated with wetting fluid, e.g., oil into water, using simulations that share the following features: three-dimensional cubic lattices of different size, pore throats represented by lattice bonds, nonwetting fluid invasion, source at the base, source pressure incremented until breakthrough, capillary pressure equilibrium, small Bond numbers, cylindrical nonperiodic boundaries, and

sample size variable. These characteristics are discussed in greater detail below. Some simulations with higher coordination number lattices, different boundary conditions, or variable aspect ratios are also discussed in later sections.

Rather than using cells with planar boundaries, cylindrical sample geometry was chosen. Cylindrical geometry defines the horizontal length scale unambiguously as the diameter. In contrast, the length scale of a square cross section is ambiguous. Lattice sizes ranged from 8 to 100 units. Most horizontal (xy) bonds at the cylindrical perimeter are terminal; a few bonds connect to vertical bonds on the cylindrical boundary. Periodic boundary conditions, which are not readily used with the cylindrical geometry, require segments that cross a vertical boundary to terminate within the structure or to be-

come part of the flow path between top and bottom surfaces. This requirement results in higher saturations and more parallel pathways compared to the case of terminating boundaries. Rather than using periodic boundaries, we prefer to generally use relatively small ratios of the numbers of surface bonds to interior bonds. Periodic boundary conditions for fluid invasion are not representative of either laboratory core plugs or the field scale problem.

Each bond in the lattice is assigned a pore throat radius that is randomly selected from a particular pore size distribution. A throat can be invaded if it is connected to a filled throat and if the invading fluid pressure P_F is greater than or equal to the capillary pressure P_c corresponding to that throat. The capillary pressure for a cylindrical pore throat of radius r is given by

TABLE I. The ranges of parameters investigated in numerical simulations of capillary invasion with buoyancy. For all runs unless noted $t = 0.02$ cm, $2\gamma \cos\theta = 623.5$ g/cm for negative buoyancy, and $2\gamma \cos\theta = 27$ g/cm for positive buoyancy.

L/h (units of bonds)	$\Delta\rho$ (g/cm^3)	r_{max} (μm)	r_{min} (μm)	m [a]
Power-law distribution with negative buoyancy				
20 to 40	-30 to -13	50	0.5	0
32	-13.54	500	5	-2.5 to 0
Power-law distribution with positive buoyancy				
40[b]	1.19	50	0.5	0
8 to 100	0 to 5	50	0.5	-2.5 to 1
16 to 50	0 to 7	500	5	-2.5 to 0
32	2 to 2.5	100	1	-2.5 to 1
20 to 32	0.75 to 1.2	125	1.25	0
32 to 50	1.2 to 2.5	20	0.2	0
32 to 50	5	250	2.5	-2.5
32	2.5	200	2	-2.5
20 to 32	1.2 to 2.5	100	0.1	0
20	1.19	100	0.01	0
20	1.19	100	0.001	0
32	2	100	500	0
32	0.75 to 1	100	200	0
20	1.19	50	0.05	0
Linear distributions				
32 to 40	0.5 to 2	50	0.5	100 to 1000
Binomial distributions[c]				
32	0.5 to 1	50	0.5	0.2 to 0.5
Power-law distribution with cubic boundaries[d]				
24.5	0 to 2	50	0.5	0
25	0 to 2	50	0.5	0
Power-law distribution with high coordination $(Z = 14)$[e]				
11 to 20	0 to 1	50	0.5	0

[a]For power-law pore size distributions m is the exponent; for linear distributions m is the ratio of the number of radius r_{min} to the number at r_{max}; for binomial distributions m is the event probability.
[b]Runs with throat length t varied from $t = 0.01$ to 0.04 cm, or $2\gamma \cos\theta = 54$ g/cm.
[c]"Number of trials" $= 500$.
[d]Cubical rather than cylindrical sample boundaries.
[e]Body-centered-cubic lattice with next nearest neighbors $(Z = 14)$; cylindrical sample boundaries.

$$P_c = \frac{2\gamma \cos(\theta)}{r} , \qquad (1)$$

where γ is the interfacial tension between the oil and water and θ the contact angle measured between the oil-water and water-pore-wall contacts. The fluid pressure at height Z is given by

$$P_F(Z) = P_0 + \Delta\rho g Z , \qquad (2)$$

where $\Delta\rho$ is the density difference between water and oil, g is the gravitational acceleration, and P_0 is the pressure at height $Z = 0$, which corresponds to the top of the source region, i.e., the base of the invaded rock. Only the pore throats are considered in this calculation; pore bodies of radii larger than the throats that connect them do not affect the criterion for nonwetting fluid invasion.

The ranges of typical parameters used in the calculations are given in Table I. The oil source is located at the cylinder base ($Z = 0$) and the lateral extent of the source spans the entire cylindrical base. The source fluid pressure at $Z = 0$ is incrementally increased. With each pressure step, the accessible pore throats (nearest neighbors to the filled structure) that can be filled, i.e., $P_c \leq P_F(Z)$, are filled. Viscous effects are ignored; it is assumed that the pores fill quasistatically. The calculation is terminated at the percolation threshold, i.e., when the oil forms the first connected path from the basal source to the upper boundary. This pressure increment method, which is also used by Fatt [12], de Gennes and Guyon [13], Maier and Laidlaw [14,15], and Ferrand and Celia [16], differs from that commonly employed in "invasion percolation" [5,8,17–19]. In invasion percolation bonds are assigned random numbers X_i between 0 and 1. The random numbers are adjusted for the effect of buoyancy through

$$R_i = X_i + Gz_i , \qquad (3)$$

where R_i is the threshold at the ith bond, z_i is the height of the bond, and G is the gravitational gradient (which is negative for the invasion of low-density nonwetting fluid into wetting fluid). At each step the invading fluid is advanced into the bond that has the lowest rank R_i among those bonds that are nearest neighbors to the invaded fluid. The chosen rank may decrease when new nearest neighbors become available. In contrast, the pressure increment method enables all accessible pores that can be filled at a certain applied pressure (rank) to be filled and injection pressure (rank) always increases with each new step. Figure 1 shows the differences that result for a simple case consisting of a two-dimensional section of sites. Without buoyancy, 25% more bonds in this case are filled by the pressure increment method [cf. Figs. 1(b) and 1(c)]. With buoyancy the ranks of the sites are reduced with elevation [Figs. 1(d) and 1(e)]. The lowest-rank method produces a lower saturation compared to the case without buoyancy, whereas for the pressure increment method the number of filled sites increases.

Our pressure increment technique is clearly a constant applied pressure technique because the invaded structure for a given run only depends on the final applied pressure. In contrast, the lowest-rank method, which is defined as

invasion percolation by Wilkinson and Willemsen [8], is an attempt to model displacement at constant flow rate. A more physically applicable model of displacement at constant flow rate would likely include fluid viscosity and hydrodynamic pressure drops directly in the invasion algorithm. The invaded pore structures for these two invasion methods are identical at the rank (pressure) required to breakthrough the critical pore. Beyond this point, they differ as the lowest available rank decreases. Because the location of the critical pore that must be filled for breakthrough is at $\sim \frac{3}{4}$ of the sample height for the cubic lattice (and lower when the invading fluid is less dense; see later discussion), more pores at higher elevations can be filled at that same injection pressure than is the case when the next lowest rank is selected. Thus, at breakthrough the pressure increment method produces a denser structure near the top of the sample that becomes more dense with increasing buoyancy.

In capillary invasion pore throats that are not connected to filled throats cannot be filled, so we do not have to treat the entire lattice in the calculation. The filling of a pore throat on a cubic lattice allows access of up to five new unfilled throats. In each run, we treat only the growing pseudolattices that consist of the nearest neighbors to the filled throats and the filled throats themselves. The
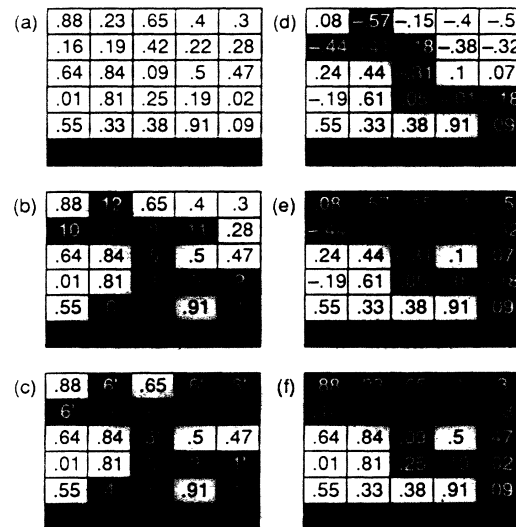

FIG. 1. Capillary invasion on a 5×5 square lattice adapted after Bunde and Havlin [19]. Values refer to the rank or resistance of sites (a) in the initial state, (b) after 12 steps of seeking lowest rank, and (c) after 6 steps of increasing the selected rank and filling all sites of rank less than or equal to the selected rank. Numbers refer to the step and primes denote sites that are subsequently filled during the same step. (d) The rank is reduced by a vertical gradient of 0.2 per cell and sites of lowest rank are filled. (e) The rank is reduced as in (d) with site filling as in (c). (f) The rank as in (a), but with a vertical gradient in fillable rank (pressure) of 0.2 per cell. Case (f) is equivalent to (e) and can be interpreted as the result of a buoyancy pressure gradient of 0.2/unit plus an injection pressure of 0.09. Saturations at breakthrough are (b) 48%, (c) 60%, (d) 36%, and (e) 64%.

number of remaining pores that are not explicitly defined in the calculation are each assigned a volume corresponding to the mean (expected) volume for a pore of a given pore size distribution. This approach has the advantage that the computer memory required to store the pore structure is significantly reduced. For example, on a 50 bond diameter, 50 bond high cylinder, the invasion can be simulated with less than 25% of the total number of throats in the complete lattice. In addition, this technique is valuable when examining the path of the oil as it migrates in space without the influence of boundary conditions. Such studies are potentially useful for understanding the spatial variability of secondary migration pathways.

We do not include effects of trapping of the wetting fluid (water) by the invading oil. At the percolation threshold in three dimensions, the saturations are low enough that trapping is rare especially for the larger sample sizes. In rocks where the coordination number may be greater than 6 (cubic) and surface roughness exists, trapping of the wetting fluid during slow drainage is likely to be even less probable at the percolation threshold. In some runs where saturation is high at the top of the sample due to buoyancy there may be trapping that is not accounted for by our model. The saturations in those cases would be reduced.

III. THE CHARACTERISTIC PORE THROAT RADIUS

The total number of tubes in the network for any given lattice size is

$$N_T \propto \int_{r_{\min}}^{r_{\max}} f(r)dr \ ,$$ (4)

where $f(r)$ is the pore size (throat radius) distribution that ranges from radius $r_{\max}$ to $r_{\min}$, which are the maximum and minimum pore sizes on the lattice. The fraction of all tubes in the network with radius larger than a particular radius r_t is

$$p = \int_{r_t}^{r_{\max}} f(r')dr' \bigg/ \int_{r_{\min}}^{r_{\max}} f(r')dr' \ .$$ (5)

For power-law pore size distributions

$$p = \frac{r_{\max}^{m+1} - r_t^{m+1}}{r_{\max}^{m+1} - r_{\min}^{m+1}} \quad (m \neq -1) \ ,$$ (6a)

$$p = \frac{\ln(r_{\max}/r_t)}{\ln(r_{\max}/r_{\min})} \quad (m = -1) \ .$$ (6b)

p corresponds to the occupation probability in ordinary percolation in which all lattice bonds less than a specified rank (i.e., greater than r_t) are occupied irrespective of whether or not the bonds lie on a path that is connected to the "source." In the case of invasion percolation, bonds can only be occupied if they are adjacent to bonds that are already occupied and hence Eq. (6) does not apply. For invasion percolation we will denote occupied bond fractions with F to distinguish them from their counterparts in ordinary percolation. The critical occupation probability in ordinary percolation p_c is the

minimum value of p when at least one path connects the bottom and top boundaries for a lattice that is randomly filled. For a simple cubic network $p_c \approx 0.2488$ [20]. At the percolation threshold $p = p_c$ and the smallest radius on the percolating cluster can be determined from Eq. (6). This radius, which we denote as r_c, is the crucial link in percolation [21]. r_c is the same for ordinary percolation and capillary invasion percolation. If it is filled, a cluster of filled pores connects the top and bottom of the sample. r_c corresponds to the characteristic length parameter l_c $(=2r_c)$ found from mercury-injection capillary pressure studies [21,22]. This radius is identified as the point of inflection of the capillary pressure curves (see Fig. 2) and marks the instant of breakthrough [23]. It is explicitly determined in the present numerical simulations. In Fig. 3 the capillary invasion simulation was allowed to continue beyond the breakthrough pressure. The simulation shows many of the same features as the experimental data including the positive curvature before breakthrough and the negative curvature after breakthrough, as well as the staircase structure. It is only necessary to reach the instant of breakthrough to determine r_c. The capillary pressure that must be attained for breakthrough is given by Eq. (1).

r_c calculated from Eq. (6) with $p = p_c$ compares well with r_c determined directly from the simulations for different power-law pore size distributions. This correspondence is independent of buoyancy and sample size over the range of parameters investigated. Although we observe that r_c decreases with decreasing buoyancy, the dependence is very weak. The relationship between r_c and the arithmetic mean $\bar{r}$ of the pore size distribution is shown in Fig. 4 for power-law pore size distributions. In general, r_c is of the order of $\bar{r}$.

At zero buoyancy, r_c (and the corresponding capillary pressure) also depends on sample geometry. r_c increases slightly with sample size for samples of aspect ratio [(height):(diameter)] 1; it decreases slightly with increasing aspect ratio (Fig. 5). These results suggest that for large sample sizes the probability that the invaded path must go through a small pore is reduced and that for high-aspect-ratio samples there is a lower probability that
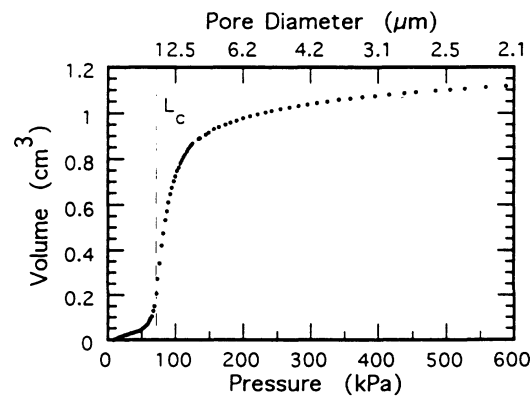

FIG. 2. Typical mercury injection curve for Berea sandstone. The inflection point is a capillary pressure corresponding to the characteristic length parameter l_c $(=2r_c)$.
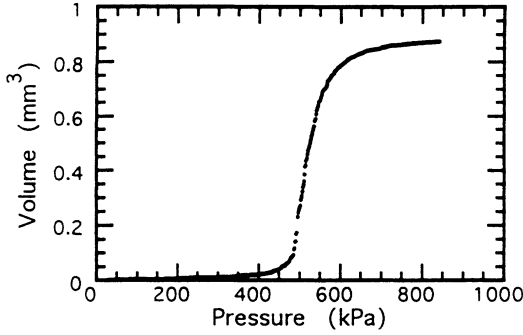
FIG. 3. Simulation of capillary pressure curve for a run with a uniform pore size distribution ($m = 0$) over the range 0.5–50 μm with $2\gamma \cos\theta = 27$ dyn/cm.
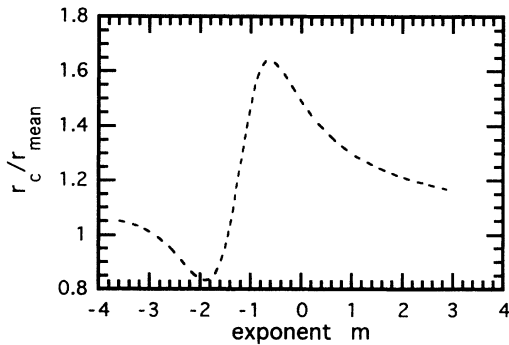

FIG. 4. Ratio of the characteristic radius r_c to the mean radius $\bar{r}$ for power-law pore size distributions $f(r) \propto r^m$ as a function of the exponent m of the pore size distribution with $r_{max}/r_{min} = 100$.
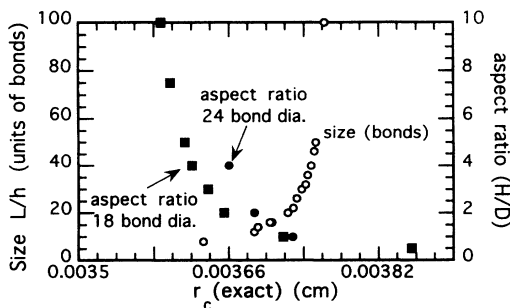

FIG. 5. The sample size in units of bonds (open circles) and the aspect ratio [(height):(diameter)] at constant diameter of 18 bonds (solid boxes) or 24 bonds (solid dots) as functions of the characteristic radius r_c.
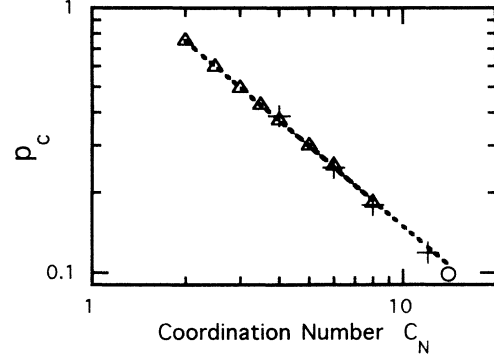
FIG. 6. Critical occupation probability for ordinary percolation p_c as a function of lattice coordination number C_N. The data are from [14] ($\triangle$), [20] ($+$), and [24,25] ($\bigcirc$). The dotted line corresponds to the relation from [26] [see Eq. (6)].

the path can avoid a small pore.

The critical percolation probability for ordinary percolation is a sensitive function of coordination number [14,20,24,25], as shown in Fig. 6. With increasing coordination number, p_c decreases according to the power law

$$p_c = \frac{d}{d-1}\left[\frac{1}{C_N}\right] = \frac{1.5}{C_N} \tag{7}$$

[26]. From $p_c(C_N)$, $r_c/r_{max}(C_N)$ can be determined from Eq. (6). Figure 7 shows r_c/r_{max} for four power-law distributions ($m = 1.5, 0, -1.5$, and -2.5) and for three pore-size-distribution windows (relative widths are r_{max}/r_{min}). With increasing coordination number, r_c moves closer to r_{max}. When $m \geq 0$, r_c/r_{max} is independent of r_{max}/r_{min}; for $m < 0$, r_c/r_{max} decreases with increasing r_{max}/r_{min}. For a given window, r_c/r_{max} increases with increasing m.
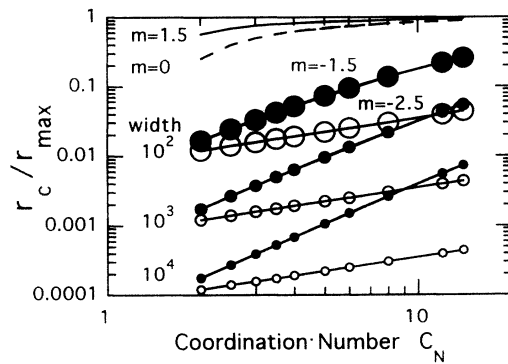

FIG. 7. Ratio of the characteristic radius to maximum radius as a function of coordination number C_N for power-law pore size distributions as determined from Eq. (6). The relative widths of the pore size distribution windows are $r_{max}/r_{min} = 10^2$, 10^3, and 10^4 and the power-law exponents are $m = 1.5, 0, -1.5$, and -2.5. For each of $m = 1.5$ (solid curve) and $m = 0$ (dashed curve), all three windows yield the same $r_c/r_{max}(C_N)$. For $m = -1.5$ (solid-dot curves) and $m = -2.5$ (open-dot curves), the dot symbols increase in size from $r_{max}/r_{min} = 10^4$ decreasing to $r_{max}/r_{min} = 10^2$.

The rate of change of r_c/r_{max}, $\partial(r_c/r_{max})/\partial C_N$ depends more strongly on m than the distribution window width. It can be concluded from Fig. 7 that for power-law pore size distributions with $m < 0$ (i.e., skewed toward the smaller pores) and $C_N > 3$, coordination number may have a smaller effect on r_c compared to the effect from the pore size distribution itself (i.e., m and r_{max}/r_{min}).

IV. EFFECT OF BUOYANCY ON CORRELATION LENGTH

In percolation theory, the correlation length ξ is defined as the average root mean square distance between occupied sites that belong to the same finite cluster [17]. It is a measure of the connectedness of filled pores at a particular occupation probability. Near the percolation threshold

$$\xi \sim (p - p_c)^{-\nu} , \tag{8}$$

where p is the occupation probability [Eq. (6)], p_c is the critical probability, and $\nu = 0.88$ for a three-dimensional lattice [20]. At $p = p_c$ we have $\xi = \infty$. Although p gives the fraction of tubes with $r \geq r_t$, the fraction of filled (occupied) tubes belonging to the percolation cluster is

$$P_\infty \sim (p - p_c)^\beta , \tag{9}$$

where $\beta \approx 0.42$ in three dimensions [19].

At breakthrough without buoyancy the correlation length is infinite and sample size $L \ll \xi$. The cluster of pores that belong to the infinite cluster is a fractal of dimension 2.5 in three-dimensional space [8]. Thus the probability that a throat belongs to the infinite (percolating) cluster is $P_\infty \sim L^{-1/2}$ for a volume proportional to L^3.

In the case of buoyancy, the length over which the fractal behavior is observed is limited by the interplay between buoyancy and capillary pressures. Wilkinson [1,2] recognized that the buoyancy pressure gradient, which causes a variation in the accessible pore fraction with height, can be equated to a gradient in occupation probability. The change in occupation probability over a correlation length cannot exceed $p - p_c$:

$$\xi \frac{\partial p}{\partial z} \sim \xi \frac{B}{h} \leq p - p_c , \tag{10}$$

where B is the Bond number, i.e., the ratio of buoyancy to capillary pressures, and h is the lattice spacing. Without such a limit, as the percolation threshold is reached the change in percolation probability over a correlation length $\xi B/h$ would be infinite no matter how small the Bond number. By combining Eqs. (8) and (10) Wilkinson [2] showed that the maximum correlation length in the pressure of buoyancy is

$$\frac{\xi_B}{h} \equiv \left[\frac{1}{B} \right]^{\nu/(\nu+1)} , \tag{11}$$

where $\nu/(\nu+1) = 0.468$. The invaded structure is fractal over a correlation length ξ_B [1,2].

V. NUMERICAL AND EXPERIMENTAL RESULTS

For most of the numerical simulations summarized in Table I the pore throat radii r are randomly distributed with a distribution function $f(r) \propto r^m$, where m ranges from 0 for uniform distributions to -2.5 for strong power laws and the pore size window ranges between r_{max} and r_{min}. Usually we chose $r_{max}/r_{min} = 100$; some wider and narrower distributions were also studied. A few binomial and linear distributions were also examined.

A. Size dependence without buoyancy

Figure 8 illustrates the result of a numerical simulation of capillary invasion on a 32-unit-height, 32-unit-diam cylinder without buoyancy. The pore throat radii are not illustrated full scale in the figure. The pores that belong to the percolating cluster that connects the basal source and the top of the sample are shown in violet. The pretender pathways, which start at the source but never reach the top, are shown in green. Typically, the maximum pretender height is less than half the sample height and their relative heights decrease with increasing buoyancy. The structures such as those shown in Fig. 8 vary considerably from run to run. Usually several hundred runs with different selections of random pore sizes are required to get adequate averages. We have not found significant improvement in the statistical averages by examining higher coordination lattices, e.g., $C_N = 14$ (body-centered cubic with next nearest neighbors). This result, in view of the fact that measurements from adjacent cores of most rocks do not exhibit wide variability in saturations, suggests that there exists long-range order among the pores in rocks.

Figure 9(a) shows the fraction of sites belonging to the percolating cluster as a function of lattice size for 1:1 aspect-ratio cylinders without buoyancy forces. Most of the points in this plot represent the average of several hundred runs (see Table I). Regardless of the pore size distribution

$$F_c(0) \propto \frac{1}{\sqrt{L/h}} , \tag{12}$$

where $F_c(0)$ is the fraction of sites belonging to the percolating cluster when buoyancy is absent ($\Delta \rho = 0$), L is the sample size, and h is the lattice spacing. The $(L/h)^{-1/2}$ dependence is expected from theory as discussed in the Sec. IV. It has also been verified by similar network simulations by Blunt, King, and Scher [9] using the lowest-rank method of invasion. The fact that ordinary percolation and invasion percolation via constant pressure or lowest-rank methods produce the same structures at zero buoyancy and that the fractal dimension of these structures depends only on the dimensionality $d = 2$ or 3 of the lattice indicates that all structures belong to the same universality class.

Figure 9(b) shows the sample size dependence of the fraction of bonds that belong to the backbone as determined by a method similar to that of Herrmann, Hong, and Stanley [27]. Only uniform pore size distributions ($m = 0$) were examined, although without buoyancy oth-

er distributions have the same dependence. The fractal dimension of the backbone D_B is 1.94 for these simulations. (We also observe the same D_B when periodic boundary conditions on cubic lattices are used.) In a similar manner, Herrmann, Hong, and Stanley [27] calculated $D_B \approx 1.77$. Other values of D_B include 1.74 (percolation cluster structure studies [28]), 1.8–2.1 (Monte Carlo simulations [29]), and 1.83 (series expansion [30]). The present value for D_B was computed for invasion percolation with pressure throughout the structure given as the breakthrough pressure. Consequently, the backbone contains additional bonds near the upper boundary compared to the cases of ordinary percolation where cluster growth stops as soon as the upper surface is contacted. The inclusion of these bonds causes a higher D_B here rel-

ative to that for most of the other estimates for ordinary percolation.

Figure 9(c) shows a similar plot for the fraction of sites F_p that occur on the pretender paths that are not connected to the percolating structure. Because there may be several isolated pretenders each of which terminate at a different height, their total volume does not follow the $1/\sqrt{L/h}$ dependence. For sample sizes greater than ~ 30 bonds, the percolating cluster accounts for $\sim 60\%$ of the total occupied pores. The simulations show that the ratio of the volume of pores on the percolating cluster to that of the pretenders is directly related to their occupancy fractions: $V_c/V_p = F_c/F_p$. This relation applies to all pore size distributions we examined. (It is also likely to apply when pore bodies are also included in the calcu-
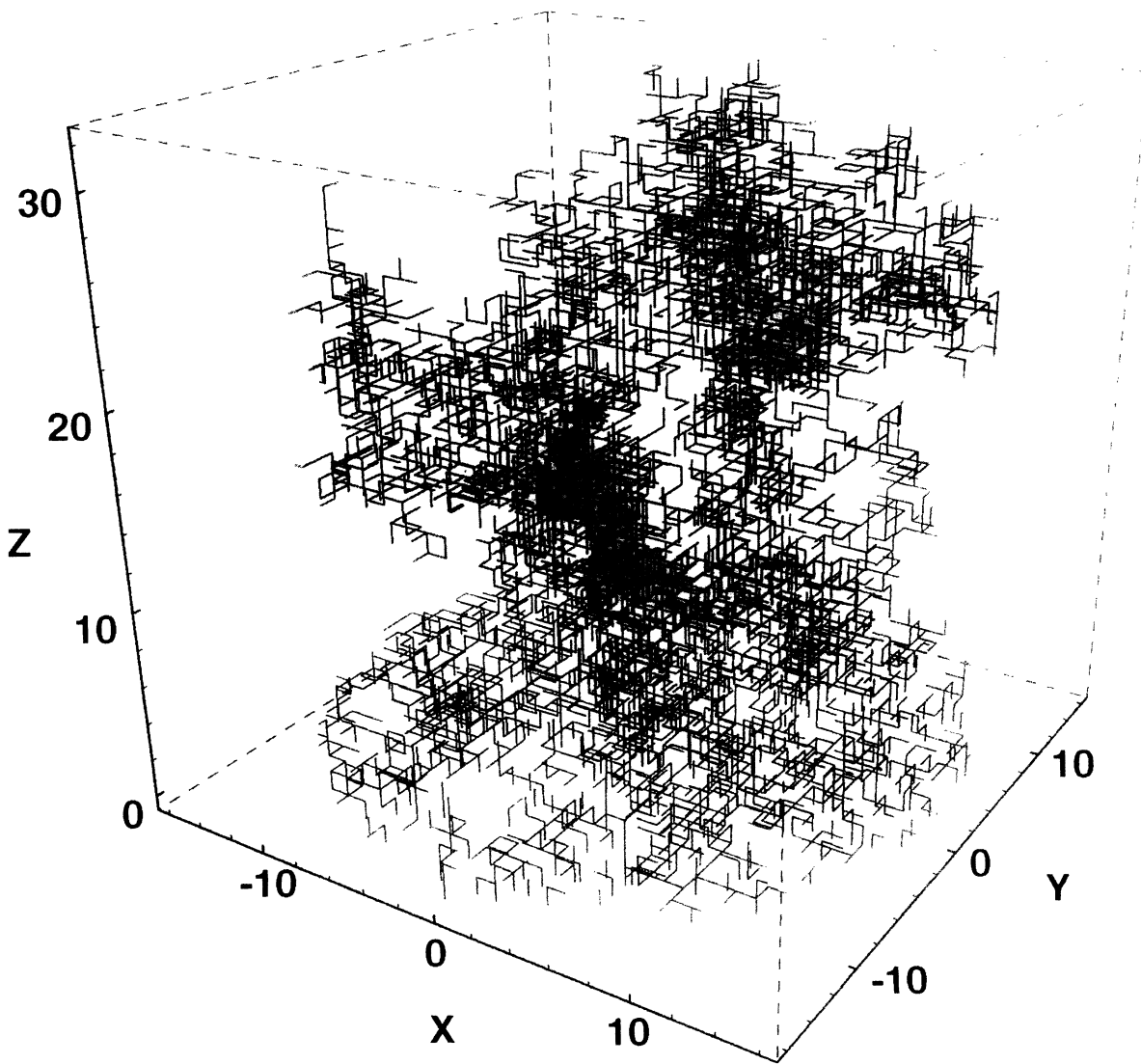

FIG. 8. Displacement pattern at breakthrough obtained from nonwetting fluid invasion on a cubic lattice from the base into a cylinder of size $\propto 32^3$. The pore size distribution is uniform, i.e., $m = 0$. The percolating structure is shown in violet and the pretenders are in green.

lation because both the pores belonging to the pretenders and the pores belonging to the percolation cluster are described by essentially the same pore throat and pore body distribution functions.) Figure 9(d) shows the total fraction of filled sites F_t, i.e., pretenders plus percolating cluster. The decrease of F_t with sample size follows $\sim (L/h)^{-0.43}$ dependence; within error, this dependence is indistinguishable from the $(L/h)^{-1/2}$ dependence. We concentrate our analyses mainly on the percolating cluster because it is more important for flow.

Figure 10 shows the results from laboratory measurements of breakthrough saturations in Berea sandstone as a function of sample size over the size range of 0.36–30 cm. The datum on the 30-cm-diam, 30-cm-high sample is the result for a slow upward invasion of tetradecane from the sample base into water filled pores. The data on smaller samples are for mercury injection from all surfaces into evacuated samples. The datum at 3 cm was common to both mercury injection and tetradecane displacing water.

Figure 11 shows breakthrough saturations from mercury invasion experiments on Coconino sandstone as a function of sample size over the size range of 0.5–2.5 cm. In contrast to Berea, Coconino sandstone has pronounced permeability anisotropy with $k \sim 10$ μdarcy along bedding planes and $k < 0.1$ ndarcy perpendicular to bedding. For two-dimensional invasion percolation, satu-

ration follows $S \propto L^{D_F-2}$, where $D_F \approx 1.89$ [8]. Two extreme invasion modes are possible in the Coconino sample. Invasion may take place dominantly along one layer of the rock. In this case the saturation at breakthrough will be small, corresponding to threshold filling of a single plane. In the second case all of the planes will be filled to the percolation threshold and the saturation at breakthrough will be typical of percolation thresholds in two dimensions, 30–50 %. The observed saturation at breakthrough of 30% indicates that all of the two-dimensional layers of these samples are partially filled at threshold. The slow change of saturation with sample size is consistent with a two-dimensional percolation problem where $S \propto L^{-0.11}$, but the scatter of the data prevents a unique measure of the exponent. The relatively large scatter of the data results from the steepness of the capillary pressure curves. The plot of saturation vs pressure for Coconino sandstone is nearly vertical near the percolation threshold, which introduces a large uncertainty in the threshold saturation.

The effect of sample aspect ratio on the occupied pore fraction at breakthrough as determined from simulations is shown in Fig. 12. At low aspect ratios, a greater volume of invaded fluid can exist in pretenders compared with the volume on the percolating cluster. In the low-aspect-ratio range, fractional occupation increases strongly with aspect ratio. At high aspect ratios, the
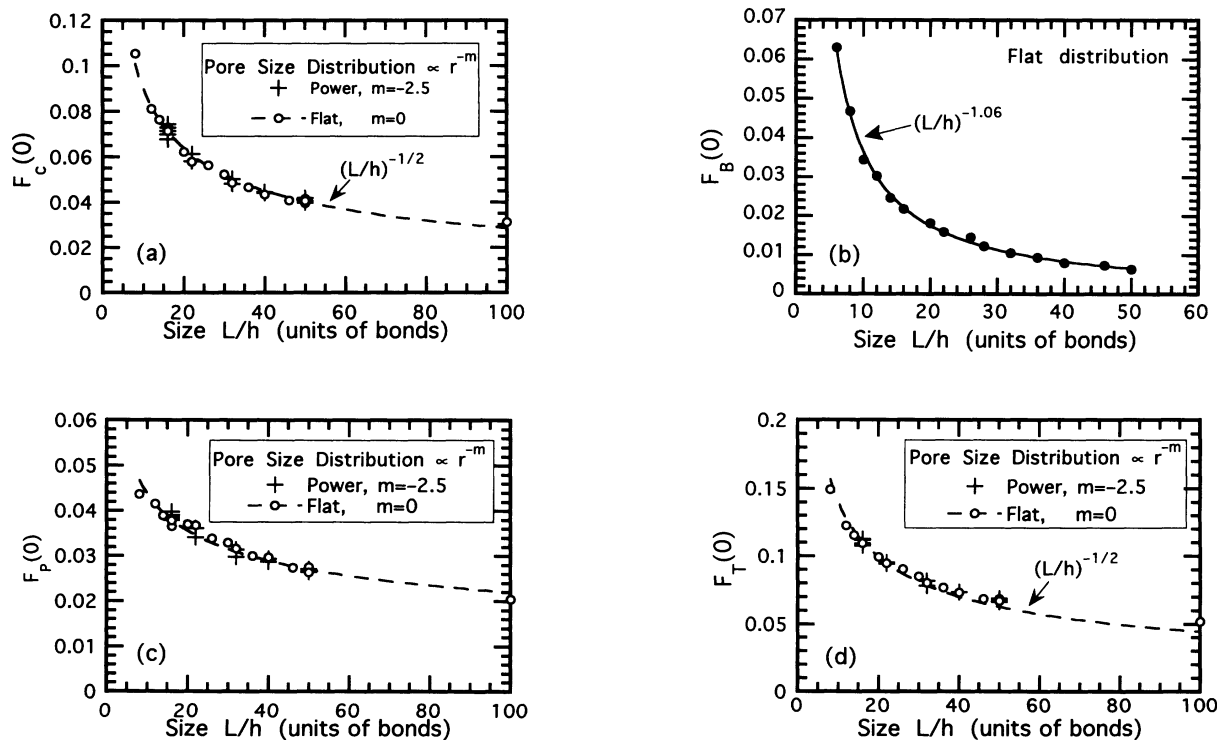

FIG. 9. Fraction of filled pores as a function of sample size (in units of bonds) for 1:1 aspect-ratio samples without buoyancy: (a) only pores on the percolating structure, (b) only pores on the backbone of the percolating structure, (c) only pores on the pretender paths, and (d) all pores. For sample sizes greater than ~ 30 bonds, the percolating cluster accounts for $\sim 60\%$ of the total pore occupancy. For the percolating structure (a), regardless of the pore size distribution, all occupation fractions data follow an $L/h^{-1/2}$ size dependence. The pretender paths follow a slightly weaker size dependence of power -0.3 to -0.4.
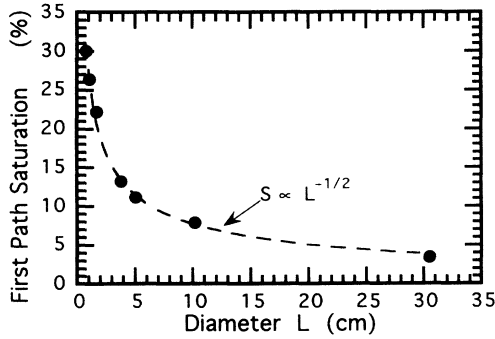
FIG. 10. Saturation at breakthrough as a function of sample diameter for Berea sandstone. The 30-cm-diam, 30-cm-high sample results are for upward invasion of tetradecane from the sample base into water filled pores. The other data are for mercury invasion from all surfaces into evacuated samples. The saturation for the 3-cm sample was also observed for tetradecane displacing water. Accuracy of measurements are within 10% of measured saturations.
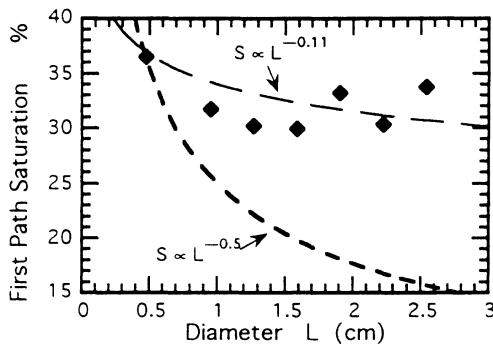

FIG. 11. Mercury invasion saturation at breakthrough as a function of sample diameter for Coconino sandstone. The curves correspond to the expected saturation dependence for two-dimensional $(\sim L^{-0.11})$ and three-dimensional $(\sim L^{-0.5})$ invasion percolation.
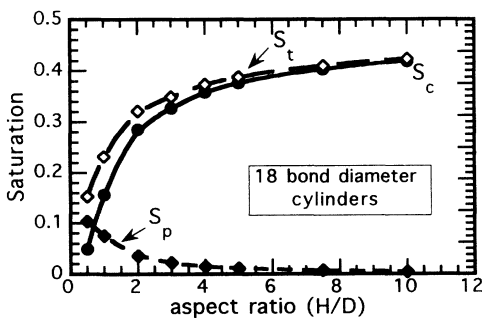

FIG. 12. Saturation at breakthrough without buoyancy as a function of aspect ratio [(height):(diameter)] from simulations of cylinders with fixed diameter of 18 bonds. Total saturation is S_T, saturation from pores on the percolating cluster is S_c, and saturation from pretenders is S_p.

dependence is very weak. Similar behavior of saturation with aspect ratio are reported for two-dimensional square lattices [3] and three-dimensional cubic lattices [31].

B. Buoyancy effects on saturation

Figure 13 illustrates the displacement pattern with buoyancy. The pattern is more dense at higher elevations compared with Fig. 8. On average, the maximum relative height of the pretenders decreases with buoyancy. This effect is most likely caused by pretenders joining the percolating cluster.

As stated earlier, the pressure increment method is more representative of cases in which fluid invasion is quasistatic and capillary equilibrium applies throughout the sample. As long as there is continuity from the source and viscous effects are negligible, the pressure at a given elevation is a simple linear function of gravity. For positive buoyancy, as the elevation in the sample increases, the probability for filling pores increases. The filled structure becomes more diffuse and funnel shaped (see Fig. 13). If pressure at the source is reduced, isolated structures can form; however, these will reconnect along the same pores when the source pressure increases again, assuming that no accompanying alteration of the rock pore structure occurred. The Bond number correlation length ξ_B defines the length scale over which the cluster is fractal [2]. We find that the largest incipient cluster at the percolation threshold, as defined by the height at which the characteristic pore r_c occurs, ξ_{r_c}, increases with increasing ξ_B (as discussed later). While ξ_B is infinite at $\Delta\rho=0$, ξ_{r_c} is finite due to finite-size effects. In addition, as shown below, ξ_{r_c} depends on sample shape.

Figure 14 shows the effect of buoyancy on the fraction of filled tubes $F_c(\rho)$ for a uniform pore size distribution at different density contrasts. For a given density contrast, e.g., curves for $\Delta\rho=0.5$ and 1.19 g/cm^3, the increase in F_c is greater for the larger lattices. As the density contrast between the nonwetting invading fluid and the wetting fluid increases, F_c increases. We observe similar behavior for the backbone portion of the percolating cluster. Figure 15 shows that for a given sample size F_c increases nonlinearly with density contrast. At small lattice size, F_c increase slowly with $\Delta\rho$; the increase for large lattices is more rapid. Initially for a given lattice size, the curvature of the F_c versus $\Delta\rho$ is positive; the extent of this behavior is greatest for small lattices. As F_c and $\Delta\rho$ continue to increase, the curvature becomes negative.

Figure 16 shows how the power-law exponent m influences the buoyancy effect at a fixed lattice size for density contrast of 2.5 g/cm^3 (Note that this density contrast is much larger than in the oil-water system.) The ordinate of this plot is the factor by which buoyancy enhances saturation, which is the ratio of the fraction of filled tubes on the percolation cluster at a density contrast of $\Delta\rho$ to the fraction when buoyancy is absent $F_c(\rho)/F_c(0)$ [see Fig. 9(a)]. The buoyancy effect is largest for the uniform distribution and for positive exponents, and its influence diminishes rapidly with in-

creasing negative power dependence. The pore size distributions of rocks are normally not uniform (flat) but are skewed toward the smaller pore sizes and thus are more likely to show negative power-law dependences. Hence we predict that network models that use uniform pore size distributions will overestimate the effects of buoyancy on saturation and relative permeability. These results also suggest that when using glass bead packs for capillary invasion experiments, the results of experiments will not be representative of those expected for rocks.

The effects of buoyancy and sample size on saturation are combined in Fig. 17. The ordinary of this plot is the same as in Fig. 16. The abscissa is L/ξ_B, which is related to material and fluid properties, size, and percolation parameters. It is given by the product of the sample size (in lattice units L/h) and the stochastic Bond number $\langle B \rangle$

(described below) raised to the power $v/(1+v)$, which is h/ξ_B. Saturation is not a unique function of Bond number but is a unique function of size and Bond number. For $L/\xi_B \lesssim 1$ we find that the invaded structure must be a fractal of dimension 2.5 because the scaling given by Eq. (12) applies within the accuracy of the data. This agrees with the theoretically expected value and lends confidence that our definition of ξ_B is correct.

The present results for all simulations of cylindrical samples with aspect ratios 1:1 indicate

$$F_c(\rho) = \frac{0.283}{\sqrt{L/h}} \left[1 + \mathcal{F} \left[\frac{L}{h} \langle B \rangle^{v/(1+v)} \right] \right]$$

$$= F_c(0) \left[1 + \mathcal{F} \left[\frac{L}{\xi_B} \right] \right] . \tag{13}$$
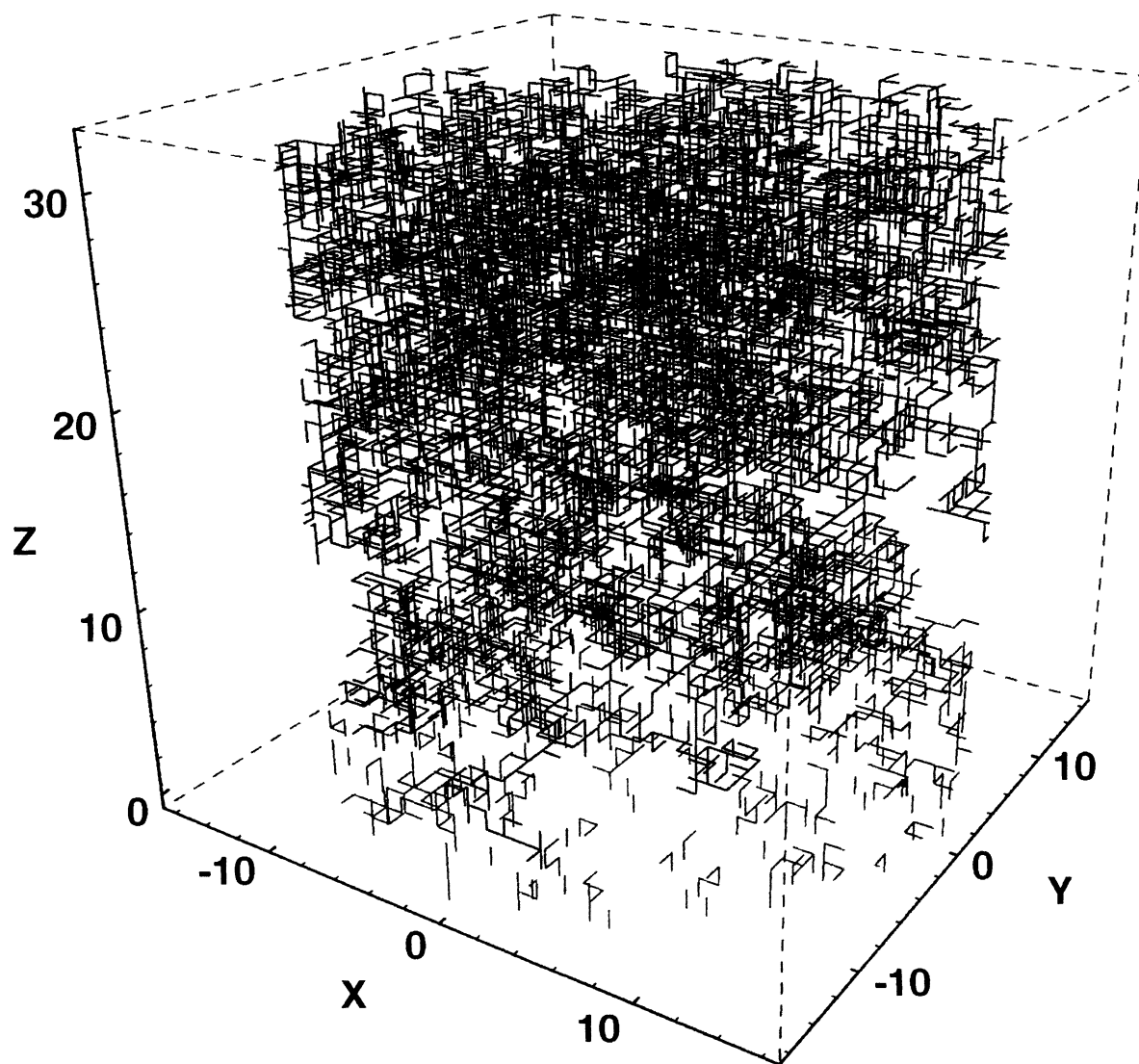

FIG. 13. Displacement pattern at breakthrough obtained from nonwetting low-density ($\Delta\rho = 1$ g/cm^3) fluid invasion on a cubic lattice from the base into a cylinder of size $\propto 32^3$. The pore size distribution is uniform, i.e., $m = 0$. The percolating structure is shown in violet and the pretenders are in green.
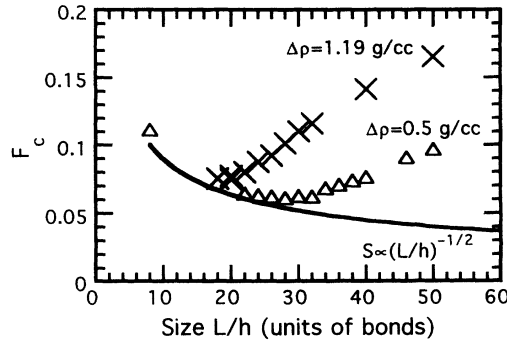
FIG. 14. Fraction of filled pores on the percolating cluster as a function of sample size with buoyancy for a uniform pore size distribution with $r_{max}/r_{min} = 100$. The $F_c \propto (L/h)^{-1/2}$ curve is the fraction when $\Delta \rho = 0$. At a constant density, e.g., $\Delta \rho = 0.5$ or 1.19 g/cm³, the occupied pore fraction initially decreases with $(L/h)^{1/2}$ at small sample sizes, but increases with sample size at large sizes.
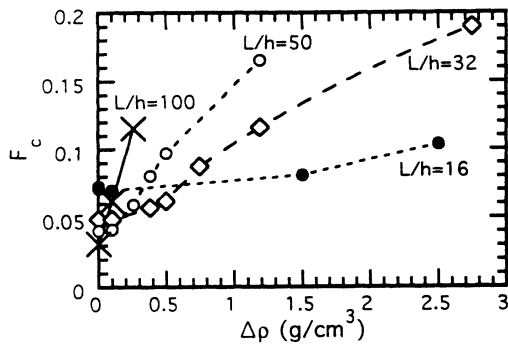

FIG. 15. Fraction of filled pores on the percolating cluster as a function of density contrast for a uniform pore size distribution with $r_{max}/r_{min} = 100$. Shown are data for sample sizes $L/h = 16, 32, 50,$ and 100.
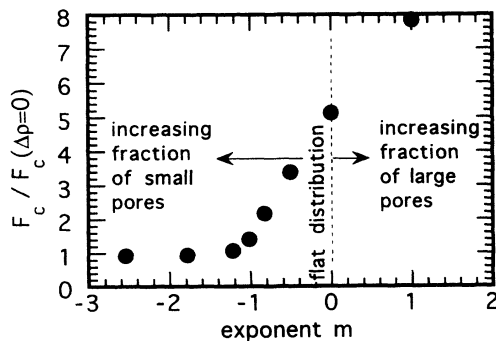

FIG. 16. Fraction of filled pores F_c normalized by the fraction without buoyancy $F_c(\Delta \rho = 0)$ as a function of the exponent m of power-law pore size distributions $f(r) \propto r^m$ at a sample size of 32 bonds and $r_{max}/r_{min} = 100$. Shown are results for $\Delta \rho = 2.5$ g/cm³. For distributions strongly skewed toward the small pore sizes, e.g., $m \leq -2$, the occupied pore fraction is nearly identical to the pore-size-independent zero-buoyancy fraction.

The functional form of $\mathcal{F}$ is not simple: $\mathcal{F} \sim 0$ and $F_c \sim L^{D_F - 3} \sim L^{-0.5}$ for $L/\xi_B \lesssim 1$. At high-density contrasts and while $L/\xi_B \gg 1$, $\mathcal{F}$ varies with $(L/\xi_B - 1)$ to the power 0.6–0.8 and $F_c \sim F_c(0)L/\xi_B$ $\sim L^{D_F - 2}B^{v/(v+1)} \sim L^{+0.5}B^{0.47} \approx (LB)^{0.5}$. Scaling up laboratory scale saturations to the field scale is a simple function of $L^{-0.5}$ at low buoyancy, where $L/\xi_B \lesssim 1$. However, because saturation depends on both $L^{-0.5}$ and L/ξ_B at higher buoyancy, scaling is more complex. Assuming that the same scaling applies to laboratory and field studies, it will be difficult to design a laboratory experiment to model buoyancy effects seen in the field. For example, scaling two orders of magnitude downward from field to laboratory size by changing the fluid properties requires a factor of 10⁴ increase in the ratio of density contrast to surface tension. Such scaling could only be achieved if the pore and grain sizes of the solid media were also changed.

Included in Fig. 17 are a few runs that represent the injection of mercury (or some other dense nonwetting fluid) into the base of an evacuated rock. Relation (13) applies also for these cases, even though buoyancy acts to enhance the saturation more toward the base of the sample. Trapping is not included in the present model. We expect that the coefficients of $\mathcal{F}$, i.e., the curvature in Fig. 17, will change with trapping.

C. Stochastic Bond number

The Bond number is defined as the ratio of the buoyancy to capillary pressures and is given by

$$B = \frac{\Delta \rho g t_{typ} r_{typ}}{2\gamma \cos(\theta)} , \tag{14}$$

where g is the interfacial tension between the wetting and nonwetting phases, θ is the contact angle, and t_{typ} and r_{typ} are the typical throat length and radius. For an arbitrary pore size distribution and structure there are no typical parameters. The Bond number must consist of statistically averaged parameters

$$\langle B \rangle = \frac{\Delta \rho g \langle t \rangle \langle r \rangle}{2\gamma \langle \cos(\theta) \rangle} , \tag{15}$$

where $\langle \ \rangle$ denote statistical or stochastic averages.

The stochastic radius $\langle r \rangle$ should reflect the range of values and the broadness of the distribution. A complete specification of a pore size distribution requires its functional form, e.g., $f(r) \propto r^m$, and the maximum and minimum radii r_{max} and r_{min}. The stochastic radius used in Fig. 17 is

$$\langle r \rangle = \bar{r} \left[\frac{r_{max}/2}{r_{max} - \bar{r}} \right]^2 , \tag{16}$$

where $\bar{r}$ and r_{max} respectively are the mean and maximum throat radii in the pore size distribution. The factor $r_{max}/(r_{max} - \bar{r})$ is the normalized inverse of the extreme deviate from the mean of the distribution. It is a constant for known $f(r)$ and known distribution window widths (i.e., $r_{max}/r_{min} = $ const). We include a factor of $\frac{1}{2}$ in the normalization of the radius in Eq. (16) so that $\langle r \rangle$
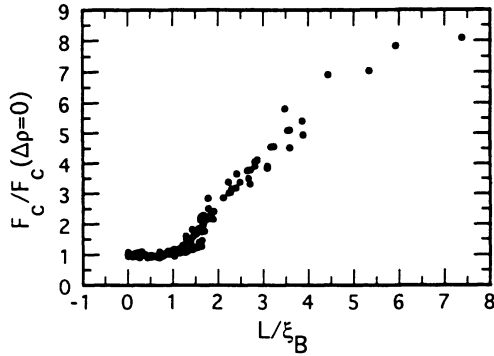
FIG. 17. The factor $F_c/F_c(\Delta\rho=0)$ by which buoyancy enhances the occupation fraction as a function of sample size and rock and fluid properties. The abscissa that scales all pore size distributions to a single curve is given by the product of the sample size L/h and a stochastic bond raised to a power that is related to the correlation exponent from percolation theory (see text for details). The abscissa is equivalent to the ratio of the sample size to the Bond number correlation length L/ξ_B. Included in this plot are positive and negative buoyancy results for power-law, uniform, linear, and binomial pore size distributions.

is approximately equal to the mean radius for a uniform ($m=0$) pore size distribution when $r_{max}\gg r_{min}$. Thus the typical radius for such distributions is the mean. For distributions that are skewed toward r_{min}, $\langle r \rangle \approx \bar{r}/4$ with $r_{min} < \bar{r} \ll r_{max}$. For distributions that are skewed toward r_{max}, $r_{min} \ll \bar{r} < r_{max}$, $\langle r \rangle$ can be much greater than $\bar{r}$. Typically, the pore size distributions of rocks are skewed toward r_{min} and buoyancy effects are less significant than for uniform pore size distributions. Figure 4 shows that for power-law pore size distributions r_c is of the order of $\bar{r}$. The Bond numbers involved in Fig. 17 for $|\Delta\rho| > 0$ are generally between 0.0001 and 0.01. The four most extreme points at $L/\xi_B > 4$ have Bond numbers between 0.01 and 0.05. The product of the Bond number and lattice height yields the ratio of the buoyancy pressure for the total sample height to the capillary pressure characteristics of the media. This product is below 0.4 for most cases and only for the most extreme point does the product exceed unity. This affirms that the results represent the capillary pressure dominated regime.

In general, both $\langle t \rangle$ and $\langle \theta \rangle$ may vary in a porous rock and will require a statistical description similar to $\langle r \rangle$. For our simulations, the throat length $\langle t \rangle$ is a constant for a given run and is equivalent to h, the lattice spacing. Similarly, $\langle \theta \rangle$ is a constant for a given run. The Bond number used in Fig. 17 has been verified for applicability to the scaling by independent variation of each of the parameters in Eq. (15). The total range of our Bond numbers is $< 10^{-5}-0.05$. The important difference between Wilkinson's ξ_B [2] and the present one is that we use the stochastic Bond number. Thus this correlation length depends on the pore size distribution function; ξ_B is larger for weak power law (e.g., $m=0$) distributions.

We examined several alternative forms for $\langle r \rangle$ including some with r_c or the geometric or harmonic mean ra-

dius. However, for the present data set that consists of different power-law, uniform, binomial, and linear distributions with window widths $2 \le r_{max}/r_{min} \le 10\,000$, none of the other forms examined came close to collapsing the data to a single curve.

D. Comparison of the scaling relation with experimental data

The laboratory measured saturations for both mercury and oil invasion at breakthrough for Berea sandstone are not significantly affected by buoyancy as indicated by their $L^{-1/2}$ dependence (Fig. 10). This implies that for these runs $L/\xi_B \lesssim 1$ or $(L/h)(\Delta\rho g \langle r \rangle^2/2\gamma \cos\theta)^{\nu/(1+\nu)} \lesssim 1$. Here we have assumed that the throat height t equals $\langle r \rangle$, but pores in Berea are not cylindrical tubes. We estimate $\bar{r}$ to be $\sim r_c$ for this rock, and because its pore size distribution is skewed toward r_{min}, $\langle r \rangle \sim \bar{r}/4 \sim r_c/4$. Thompson, Katz, and Krohn [32] report $r_c \approx 8$ μm. The normalization of the sample size L, i.e., lattice spacing h, is taken as the grain size ~ 0.03 cm. With $\gamma_{oil}=52.7$ dyn/cm, $\gamma_{Hg}=485$ dyn/cm, $\Delta\rho_{oil}=0.2372$ g/cm^3, $\Delta\rho_{Hg}=13.54$ g/cm^3, $\theta_{oil}\approx 0°$, and $\theta_{Hg}\approx 180°$, the Bond numbers are $B_{Hg}\approx 5.5\times 10^{-7}$ and $B_{oil}\approx 8.8\times 10^{-8}$, and L/ξ_B for both the largest mercury-injected sample (10 cm) and the 30-cm oil-injected sample is less than 0.5. This suggests that for samples of similar fluid and rock properties, buoyancy only will begin to affect saturation in samples that are at least twice as large as those measured.

For the oil invasion experiment, the buoyancy column height at which the buoyancy pressure equals the capillary pressure corresponding to r_c in Berea sandstone is 5.7 m. But the simulations indicate that buoyancy will affect saturation in Berea injected with oil at a height above 60 cm or one-ninth of the buoyancy column height. The buoyancy column height should not then be used as an indicator for when buoyancy is important. Our estimate of buoyancy effects depends on the accuracy of the mean radius, which is not high. Nonetheless, the results illustrate that buoyancy affects the saturation long before the buoyancy pressure is comparable to the breakthrough capillary pressure.

E. Height of the characteristic pore

For each simulation, the height of the invading oil cluster at the pressure just prior to the filling of the characteristic pore r_c was determined. This height ξ_{r_c} corresponds to the maximum cluster height before breakthrough. ξ_{r_c}/L also scales with L/ξ_B as shown in Fig. 18. With increasing buoyancy ξ_{r_c}/L decreases, i.e., the characteristic pore that must be filled at breakthrough occurs at lower heights. r_c increases (and the corresponding capillary pressure decreases) weakly with increasing buoyancy. The opposite trend applies for negative buoyancy (i.e., dense nonwetting fluid invasion). The applied pressure at the source for breakthrough shows no detectable trend with buoyancy. Without buoyancy $\xi_{r_c}^0/L \approx 0.73\pm 0.03$ regardless of the pore size distribu-
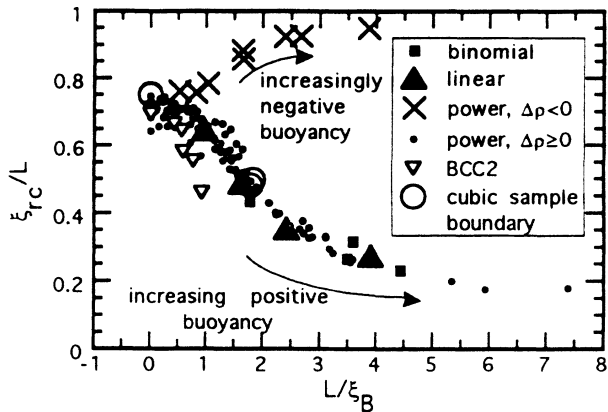
FIG. 18. Relative height ξ_{r_c}/L at which the breakthrough pore with diameter r_c exists. ξ_{r_c}/L depends on the pore size distribution and buoyancy. It scales with L/ξ_B in a manner similar to the occupation probability. The few points for the uniform distribution that fall beneath the curve are from the smallest sample sizes and are too strongly affected by finite-size effects. The points from a simulation on a body-centered-cubic lattice with next nearest neighbors $C_N = 14$ differ from the main curve as a result of their relatively higher correlation lengths ξ_B. For negative buoyancy $\Delta\rho < 0$, for example, in mercury injection, the height of the characteristic pore increases with buoyancy and sample size. Included in this plot are results from power-law and uniform (positive, O; negative mercurylike, X), linear ($\blacktriangle$), and binomial ($\blacksquare$) pore size distributions as well as results for body-centered-cubic lattices with next nearest neighbors (BCC2, ∇) and runs where sample boundary was a cubic (O).

tion. Figure 19 shows that the maximum pretender height ξ_p/L has a similar trend with L/ξ_B. ξ_p/L is less than half of the height of the sample at zero buoyancy. The pretender heights decrease with increasing buoyancy and sample size. 1:1 cubical-shaped samples follow similar dependences for ξ_{r_c}/L and ξ_p/L. For negative buoyancy, ξ_p/L is reduced relative to positive buoyancy rath-
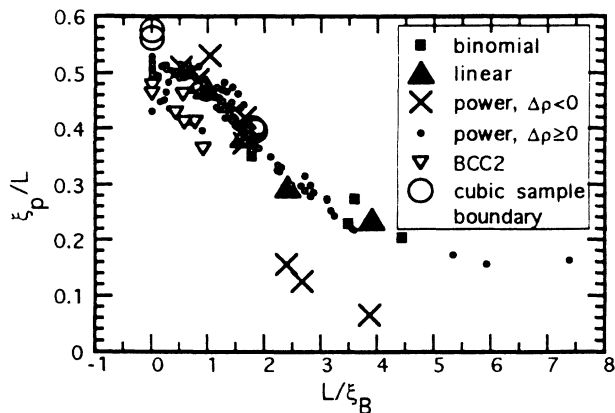
er than increased as ξ_{r_c}/L because of the greater concentration of filled pores toward lower elevations.

Because ξ_{r_c} is the maximum cluster size prior to breakthrough, it can be related to the Bond number correlation length, which represents the length over which the structure is fractal. Figure 20 shows that for $\xi_B/L \lesssim 0.6$ ($L/\xi_B \gtrsim 1.6$) both ξ_{r_c}/L and ξ_p/L vary approximately linearly with ξ_B. For high buoyancy (small ξ_B/L) and $\Delta\rho > 0$, $\xi_{r_c} \sim \xi_B$. The dependence of ξ_{r_c} on ξ_B as well as the size of r_c are identical for the lowest-rank and pressure increment methods of invasion because both methods have identical properties as the percolation threshold is approached.

The behaviors of the maximum pretender height and the height of r_c with sample aspect ratio are linked to the variations in saturation. At zero buoyancy with increasing sample aspect ratio, the relative height of r_c, $\xi_{r_c}^0/L$, and the maximum relative pretender height ξ_p^0/L decrease (Fig. 21). At low aspect ratios, there can exist many pretenders that nearly reach the top surface. As the aspect ratio increases, it is more likely that pretenders will join to the percolating cluster and thus their maximum height decreases while the percolating cluster saturation becomes a larger fraction of the total saturation. The addition of path components on the percolating cluster from pretenders makes it more likely that the height of the constriction on the first path ξ_{r_c}/L will decrease in

FIG. 19. Maximum relative height ξ_p/L of the pretender paths as a function of L/ξ_B. Plot symbols are the same as in Fig. 18.
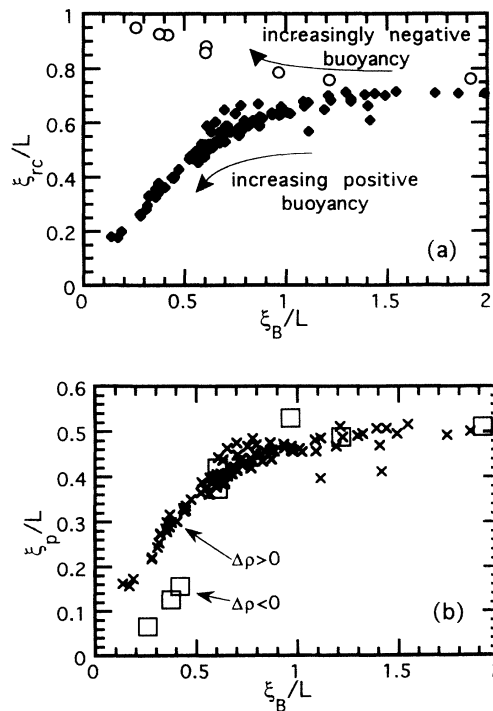

FIG. 20. Maximum relative heights (a) ξ_{r_c}/L for r_c and (b) ξ_p/L of the pretenders for $\Delta\rho > 0$ and $\Delta\rho < 0$ as functions of L/ξ_B. Results shown for positive buoyancy ($\blacklozenge$) and negative buoyancy (O). Results for the body-centered lattice are not shown.
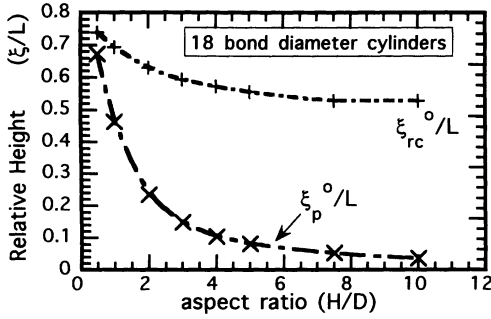
FIG. 21. Relative heights of the characteristic pore $\xi_{r_c}^0/L$ and the highest pretender ξ_p^0/L at breakthrough without buoyancy as a function of aspect ratio [(height):(diameter)] from simulations of cylinders with fixed diameter of 18 bonds.
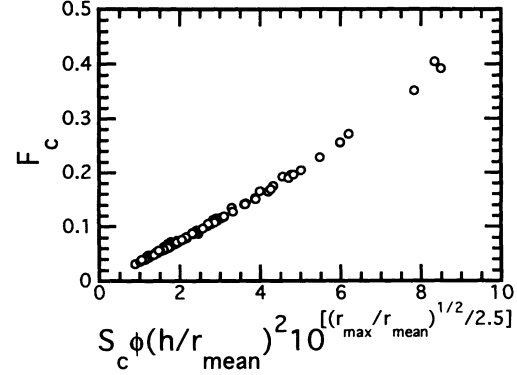

FIG. 22. Occupation fraction of filled pores on the percolating cluster for power-law pore size distributions as a function of the product of saturation from these pores, porosity, and scaling factors related to the width of the pore size distribution. See text for details.

elevation. The relative size of r_c decreases with aspect ratio so that the total percentage of pores of size $r \geq r_c$ (i.e., the saturation) increases. At large aspect ratios, $\xi_{r_c}^0/L$, ξ_p^0/L, r_c, and saturation do not change significantly with aspect ratio. Simulations involving a few different pore size distributions and different diameter samples suggest that the limit of $\xi_{r_c}^0/L$ at high aspect ratio is ~ 0.5.

Preliminary results for 1:1 cylinders of coordination number $C_N = 14$ (body-centered cubic with next nearest neighbors) show that $\xi_{r_c}^0/L \approx 0.77$, indicating no strong dependence on C_N at zero buoyancy. ξ_{r_c}/L decreases strongly with buoyancy when $C_N = 14$ over the range $0 \leq L/\xi_B \leq 2$ (Fig. 16). This sensitivity to buoyancy results from the larger correlation length for the $C_N = 14$ samples. For identical conditions the ratio of $L/\xi_B(C_N = 14)$ to $L/\xi_B(C_N = 6)$ is about 0.5, which is of the order of the inverse of the ratio of their corresponding coordination numbers. (As the $C_N = 14$ lattice has six bonds of throat length h and eight bonds of size $\sqrt{3}/2h$, the average $\langle t \rangle$ should be slightly reduced and would aid in the correspondence.) The occupancy fractions for the $C_N = 14$ lattice are smaller than the corresponding $C_N = 6$ lattice. This behavior is consistent with Fig. 17, which shows that saturation increases with decreasing buoyancy correlation length ξ_B.

F. Saturation vs percolation probability

To compute saturations from the fraction of occupied pore throats, we must account for the volume of all pore throats that exist in the lattice. The total volume of throats includes the volume contributions of throats on the percolation cluster and pretender paths that are filled, unfilled nearest neighbors to these throats, and unfilled non-nearest-neighbor throats. The volume contribution of the non-nearest-neighbor throats is determined from the product of their number and the expectation of their volume E(volume), where

$$E(\text{volume}) = \pi t \int_{r_{min}}^{r_{max}} r^2 f(r) dr . \tag{17}$$

For cylindrical pore tubes of power-law radius distribution,

$$E(\text{volume}) = \pi t \alpha_2 , \tag{18}$$

where α_2 is the second moment of the pore size distribution. For a given pore size distribution, the porosity is independent of sample size. However, as Eq. (17) shows, porosity varies with r_{min}, r_{max}, and $f(r)$. When porosity results solely from cylindrical pore throats, the empirical relationship between the occupation fraction F_c and the saturation S_c is

$$F_c \propto S_c \phi \left[\frac{t}{r_{max}} \right]^2 10^{(r_{max}/\bar{r})^{1/2}/2.5} \tag{19}$$

(see Fig. 22). The t/r_{max} term scales pore size distributions that differ only in location of the distribution window or in the pore throat length. The scale factor involving r_{max} and $\bar{r}$ is a constant for a given power law and pore size distributions width. Between fundamentally different pore size distributions, e.g., binomial and power-law, we have not found a simple relation between F_c and S_c.

In the extreme case where pore bodies with sizes uncorrelated to pore throats exist and their volume dominates, we expect $F_c = S_c \phi$. For high-porosity rocks, the total porosity may be much greater than the throat porosity and the behavior of the occupation fraction and the saturation are synonymous. In many low-porosity rocks, however, pore bodies and pore throats may be difficult to distinguish and a scaling related to with characteristics of the pore size distribution, such as in Eq. (19), is required.

G. Relative permeability and size dependence

As indicated in Fig. 10, the minimum saturation for nonwetting fluid to form a continuous path depends on sample size. Because the set of pores that are filled at this minimum saturation are among the largest pores avail-

able, we expect that properties that depend on the size and connectivity of the pore conduits, such as permeability, will also depend on sample size. We obtained preliminary experimental results for relative permeability of Berea sandstone at breakthrough in primary drainage for two different sample geometries. One sample is an 8:1 aspect-ratio, 30.5-cm-long, 3.81-cm-diam cylinder. The other sample is a 1:1 aspect-ratio, 30.5-cm-high, 30.5-cm-diam cylinder. The 8:1 cylinder was an experiment in which helium invaded an oil saturated sample [33]. The 1:1 cylinder was oil invasion into water-saturated rock. The rate of flow of invading fluid for the 8:1 cylinder was about three orders of magnitude greater than for the 1:1 cylinder. The absolute water permeabilities for these two samples was about 200 mdarcy. The minimum saturation for the 8:1 sample was $\sim 12\%$ whereas the 1:1 sample had a saturation of $\sim 3\%$. The 1:1 sample result was found to be repeatable on a similar piece of Berea sandstone of the same dimensions. The high saturation for the 8:1 sample is a result of both the high aspect ratio (see Fig. 11) and the smaller diameter. The 8:1 sample has a saturation that is more typical of a 1:1 aspect ratio of size comparable to the 3.81 cm diameter of the 8:1 sample rather than the 30.5 cm length.

At minimum nonwetting phase saturation the relative permeability of the 8:1 sample is about 0.006, which is half an order of magnitude below that of the 1:1 sample (0.019). The permeability reduction is qualitatively consistent with the numerical simulations. While the saturation is higher for the 8:1 sample at breakthrough, the characteristic pore radius (capillary pressure) required for breakthrough is smaller (larger) relative to the 1:1 sample. The pores filled in the 1:1 aspect ratio sample are among the larger pores in the rock and thus they are responsible for relatively high permeability. In addition, in the 8:1 sample many pores are filled that intersect the sample boundaries and hence do not contribute to flow. These boundary-imposed dead ends contribute to a lower permeability at a higher saturation than the 1:1 sample.

VI. COMPARISONS WITH OTHER STUDIES

The present results are in marked contrast to those of Meakin et al. [4,5], who used the lowest-rank method for invasion. The simulations of Meakin et al. show no significant change in pore occupancy with elevation. The three-dimensional structure created by their method consists of a string of blobs, each of length $\sim \xi_w$, that form an upward directed walk. The internal structure of the blobs is like that of an invasion percolation cluster with a fractal dimension of $D_F \approx 2.5$. The distance between the blobs is comparable to the blob size. The size of the blobs follows a similar dependence on Bond number as ξ_B in Eq. (11), which yields lower saturations with increased buoyancy. Meakin et al. used lattices of aspect ratio 2:1 with periodic boundary conditions. They did not do detailed investigations of pore size distribution effects on the Bond number. Their results show that with increasing gravitation gradient the structure is less diffuse and narrower throughout the sample volume. This narrowing of the filled structure is due to their choice of the lowest-

rank method.

Frette et al. [6] performed experiments involving the invasion of sucrose solutions into a random packing of 2-mm cylindrical grains saturated with dibutylphthalate. The invaded structures produced resembled those of the simulations of Meakin et al. [5], i.e., blobs on a string. However, their experiments were not in capillary equilibrium as the injection rates were high and the time required for their structures to relax was much longer than the duration of the experiment. Because of their large grain size and relatively high Bond numbers of 0.015–0.75, buoyancy pressure exceeded the capillary pressure in their experiments at corresponding heights of 65 and 2 grains. The packings were held in a cylinder 140 grains high. Whenever the filled column height exceeded the local capillary pressure, a large segment of structure could potentially disconnect and drain upward; such phenomena are reported by Frette et al. [6]. In contrast, our simulations and experiments involved samples of sizes where the buoyancy pressure at the top of the sample did not exceed the capillary pressure.

Catalan et al. [7] examined the migration of oil ($\Delta \rho = 0.239$ g/cm^3, $\gamma = 31.4$ dyn/cm) into a water-saturated, 63-cm-long, 1.9-cm-diam column packed with glass beads or quartz sand. At the start of their experiment, the base of the column was saturated with oil to a specified height. They observed that migration could occur without additional applied pressure if the height of the oil column ranged from 7 to 16 cm. These heights are much lower than the height of the sample and indicate that large Bond numbers apply. In contrast, for our oil injection experiments on 30-cm-long, 30-cm-diam Berea sandstone cylinders, the buoyancy pressure at the top of the rock was below 1% of the capillary pressure corresponding to r_c. The results of Catalan et al. suggest that saturations in secondary migration should be of the order of 10%. However, the present study shows that the geometry used in the experiments of Catalan et al. is not representative of the field. The high aspect ratios of their samples force saturations to be high and independent of sample size. In addition, their Bond numbers are not appropriate to the field.

Critical saturations of about 10% are also suggested from Schowalter's [34] measurements of capillary invasion of nitrogen into water-saturated sedimentary rocks or from mercury invasion. These samples were of the order of 2.54 cm. Saturations of the order of 10% are also observed for our Berea sandstone samples of this size. Comparison of Schowalter's results for chips of various sizes with cores shows that critical saturation tends to decrease as sample size increases. The sample sizes are not described in detail and the capillary pressure data points are too widely spaced near breakthrough to be able to determine quantitative dependences.

Earlier studies of size-dependent capillary pressure did not make use of the scaling relations intrinsic to percolation theory. Larson and Morror [35] discussed size effects in capillary pressure in terms of accessibility of pores. They found that porous media larger than a few tens of grains in size produced sharp capillary pressure curves similar to infinite samples. But at the time of that

work the definition of the percolation threshold at the inflection point of the capillary pressure curve was not widely recognized, so exact saturations at threshold were not defined. Larson and Morrow review other early work on the subject.

VII. SUMMARY

For quasistatic invasion under capillary equilibrium the critical fraction of filled pores at breakthrough decreases with the square root of sample size without buoyancy, independent of the pore size distribution. For large sample sizes, the percolating cluster accounts for ~60% of the total occupied pores and the remainder resides on pretender paths that lead from the source but are not connected to the percolating cluster. Saturation, which depends on the pore size distribution, follows a similar dependence on sample size; this has been verified by experiments on Berea sandstone over the range of sample sizes from 0.3 to 30 cm. Because saturation depends on sample size, laboratory measurements should not in general be used to estimate field saturations without including a size correction.

The inverse square root dependence of saturation on sample size indicates that the invasion process is a percolation process and that the fractal dimension of the percolation cluster is 2.5. This fractal dimension, which was obtained under the assumption of capillary equilibrium throughout the sample volume, is identical to that obtained by others in the nonequilibrium invasion percolation (constant flow rate) process. As a percolation process, the size dependence of saturation is an inherent characteristic of statistically homogeneous, random media. For a rock that has profound permeability anisotropy, such as Coconino sandstone, we observe a weaker dependence of breakthrough saturation on sample size that is consistent with two-dimensional invasion percolation.

Sample shape affects saturation at breakthrough. Large-aspect-ratio [(height):(diameter)] samples have greater saturation and smaller critical pore radius than low-aspect-ratio samples. At high aspect ratios, the dependence of saturation on aspect ratio is weak. The aspect-ratio effects are important to consider when designing and interpreting laboratory experiments as well as behavior in the field. Relative permeability at breakthrough, which is dependent on the largest interconnected pores, also depends on sample size and shape.

When buoyancy is significant the pore size distribution affects the pore occupancy and the critical saturation depends on buoyancy. These effects can be understood by including a measure of the skewness of the pore size distribution in the Bond number and combining with invasion percolation theory. Saturation does not scale with Bond number but scales with the ratio of sample size L to Bond number correlation length ξ_B, which is inversely related to the Bond number to the 0.47 power. The height of the critical pore that must be filled to achieve breakthrough also scales with L/ξ_B. Most rocks have pore size distributions that are skewed toward smaller pore sizes; this reduces the effect of buoyancy on saturation as compared with a uniform pore size distribution. Often for simplicity, laboratory experiments use relatively uniform (flat) pore size distributions (e.g., uniform glass bead packs) with the result of large buoyancy effects. Laboratory experiments must be carefully designed to account for the effect of pore size distribution on Bond number when attempting to apply such results to the field scale. Our results at small Bond numbers (capillary pressure dominated regime) are more characteristic of problems in secondary migration and possibly critical gas saturation than the usual invasion percolation simulations because capillary pressures in the field are typically larger than those observed in laboratory experiments and simulated in invasion percolation.

The same scaling that is observed for any quasistatic nonwetting fluid injection process, i.e., oil into water, gas into oil, or gas into water, also applies to mercury injection into an evacuated sample. In all these cases, the same threshold pore size r_c, as determined by breakthrough pressure, will result, which is relatively insensitive to sample size [32]. However, the saturations at threshold will be strongly size dependent. Consequently, the capillary pressure-saturation curves from different experiments cannot be simply compared when there is a large difference in size of samples. Different techniques may be more applicable to different ranges of sample sizes, e.g., mercury injection is most likely to be done on small samples, while centrifuge measurements are usually done on larger samples. There may then be differences in capillary pressure curves that have been attributed to differences in technique that are more properly ascribed to sample size effects.

ACKNOWLEDGMENTS

[1] D. Wilkinson, Phys. Rev. A 30, 520 (1984).

[2] D. Wilkinson, Phys. Rev. A 34, 1380 (1986).

[3] R. Chandler, J. Koplik, K. Lerman, and J. F. Willemsen, J. Fluid Mech. 119, 249 (1982).

[4] P. Meakin, A. Birovljev, V. Frette, J. Feder, and T. Jøssang, Physica A 91, 227 (1992).

[5] P. Meakin, J. Feder, V. Frette, and T. Jøssang, Phys. Rev. A 46, 3357 (1992).

[6] V. Frette, J. Feder, T. Jøssang, and P. Meakin, Phys. Rev. Lett. 68, 3164 (1992).

[7] L. Catalan, F. Xiaowen, I. Chatzis, and F. A. L. Dullien, Am. Assoc. Pet. Geol. Bull. 76, 638 (1992).

[8] D. Wilkinson and J. F. Willemsen, J. Phys. A 16, 3365 (1983).

[9] M. Blunt, M. J. King, and H. Scher, Phys. Rev. A 46, 7680 (1992).

[10] H. Dembicki, Jr. and M. J. Anderson, Am. Assoc. Pet. Geol. Bull. 73, 1018 (1989).

[11] J. Wei, M. A. Dahmani, and D. P. Ahlfeld, EOS Trans. Am. Geophys. Union 74, 150 (1992).

[12] I. Fatt, Petr. Trans. AIME 207, 114 (1956).

[13] P. G. de Gennes and E. Guyon, J. Mec. 17/3, 403 (1978).

[14] R. Maier and W. G. Laidlaw, J. Stat. Phys. 62, 269 (1991).

[15] R. Maier and W. G. Laidlaw, Math. Geol. 23, 87 (1991).

[16] L. A. Ferrand and M. A. Celia, Water Resour. Res. 8, 859 (1992).

[17] J. Feder, *Fractals* (Plenum, New York, 1988).

[18] L. Furuberg, J. Feder, A. Aharony, and T. Jøssang, Phys. Rev. Lett. 61, 2117 (1988).

[19] A. Bunde and S. Havlin, in *Fractals and Disordered Systems*, edited by A. Bunde and S. Havlin (Springer-Verlag, New York, 1991), pp. 49–95.

[20] D. Stauffer and A. Aharony, *Introduction to Percolation Theory* (Taylor and Francis, London, 1992).

[21] A. J. Katz and A. H. Thompson, Phys. Rev. B 34, 8179 (1986).

[22] A. J. Katz and A. H. Thompson, J. Geophys. Res. 92, 599 (1987).

[23] A. H. Thompson, A. J. Katz, and R. A. Raschke, Phys. Rev. Lett. 58, 29 (1987).

[24] M. P. Hollewand and L. F. Gladden, J. Phys.: Condens. Matter 4, 5757 (1992).

[25] G. R. Jerauld, L. E. Schriven, and H. T. Davis, J. Phys. C 17, 3429 (1984).

[26] V. A. Vyssotsky, S. B. Gordon, H. L. Frisch, and J. M. Hammersley, Phys. Rev. 123, 1566 (1961).

[27] H. J. Herrmann, D. C. Hong, and H. E. Stanley, J. Phys. A 17, L261 (1984).

[28] H. J. Herrmann and H. E. Stanley, Phys. Rev. Lett. 53, 1121 (1984).

[29] S. Kirkpatrick, in *Electrical Transport and Optical Properties of Inhomogeneous Media*, AIP Conf. Proc. No. 40, edited by J. C. Garland and D. B. Tanner (AIP, New York, 1978), pp. 99–117.

[30] D. C. Hong and H. E. Stanley, J. Phys. A 16, L475 (1983).

[31] R. P. Ewing and S. C. Gupta, Water Resour. Res. 29, 3169 (1993).

[32] A. H. Thompson, A. J. Katz, and C. E. Krohn, Adv. Phys. 36, 625 (1987).

[33] J. D. Kuzan (unpublished).

[34] T. T. Schowalter, Am. Assoc. Pet. Geol. Bull. 63, 723 (1979).

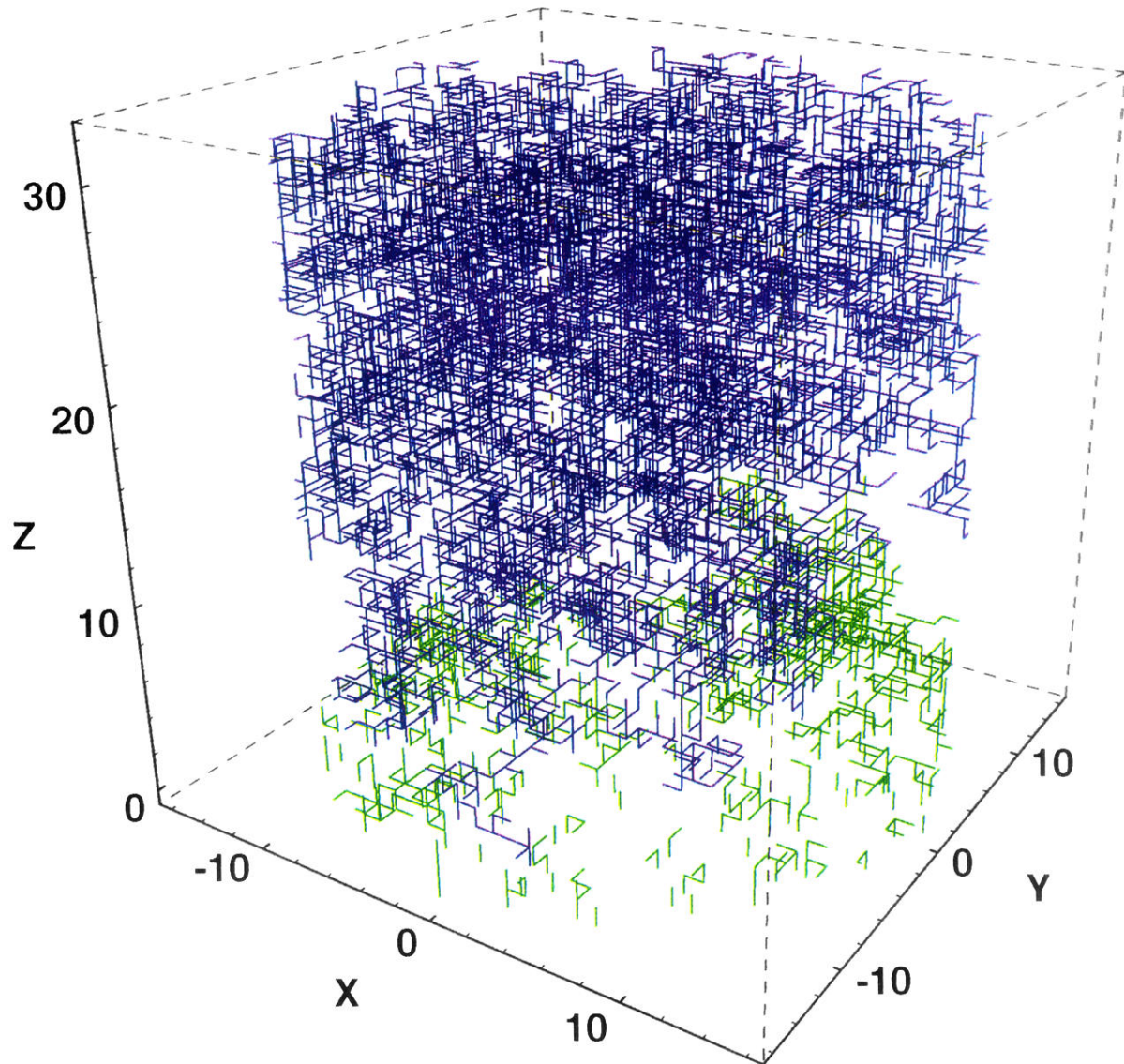[35] R. G. Larson and N. R. Morrow, Powder Technol. 30, 123 (1981).

FIG. 13. Displacement pattern at breakthrough obtained from nonwetting low-density ($\Delta\rho=1$ g/cm^3) fluid invasion on a cubic lattice from the base into a cylinder of size $\propto 32^3$. The pore size distribution is uniform, i.e., $m=0$. The percolating structure is shown in violet and the pretenders are in green.
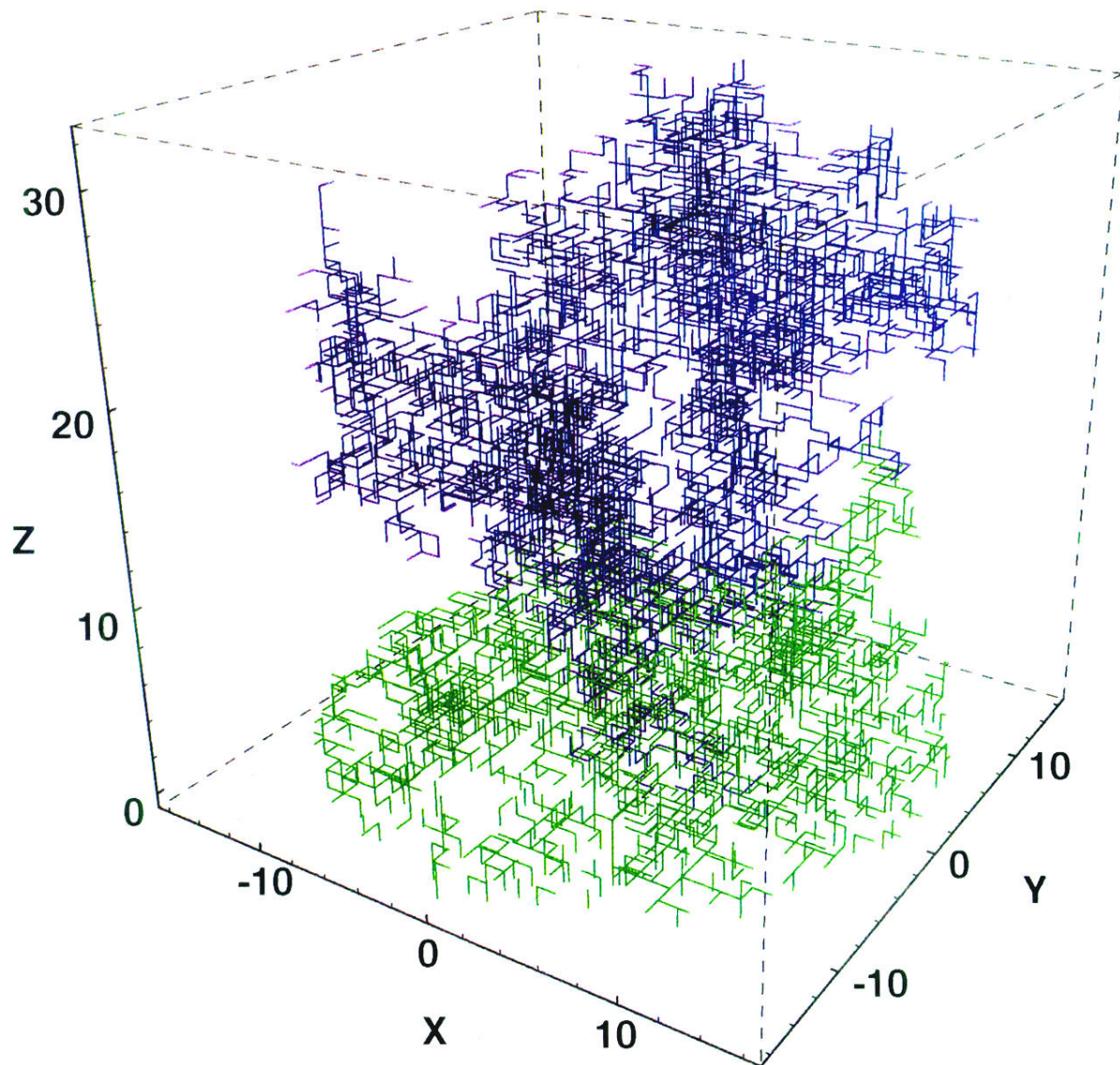
FIG. 8. Displacement pattern at breakthrough obtained from nonwetting fluid invasion on a cubic lattice from the base into a cylinder of size $\propto 32^3$. The pore size distribution is uniform, i.e., $m = 0$. The percolating structure is shown in violet and the pretenders are in green.